Mechanical Alloying of Optimised $Mg_2(Si,Sn)$ Solid Solutions: Understanding Phase Evolution and Tuning Synthesis Parameters for Thermoelectric Applications

Aryan Sankhla[‡†*], Akash Patil[‡†], Hasbuna Kamila[†], Mohammad Yasseri[†,‖], Nader Farahi[†], Eckhard Müller[†,‖], Johannes de Boor[†*]

[†]Institute of Materials Research, Linder Höhe, German Aerospace Center (DLR), D – 51170 Köln, Germany
[‖]Institute of Inorganic and Analytical Chemistry, Justus Liebig University of Giessen, D – 35392 Giessen, Germany

KEYWORDS high energy mechanical alloying, $Mg_2Si_{1-x}Sn_x$ solid solutions, solid-state reaction, thermoelectric properties.

ABSTRACT: Mechanical alloying by high energy ball milling is an attractive solid – state technique for synthesizing a diverse range of equilibrium and non-equilibrium phase materials. We have studied the synthesis of n – type thermoelectric $Mg_2Si_{0.4}Sn_{0.6}$ solid solution, aiming for a fundamental understanding of the mechanisms underlying this synthesis technique. The investigations on powders by XRD and SEM show that milling leads to welding of Mg and Sn but fracturing of Si. This fractured Si diffuses into the ductile matrix on longer milling times resulting in a phase mixture close to the nominal starting composition after 35h of milling. However, single phase pure material was only achievable after sintering, hence the synthesis of $Mg_2(Si,Sn)$ is a two – step process. Furthermore, a thorough study on the effect of varying synthesis parameters on the thermoelectric properties was performed. No strong influence of milling time on the thermoelectric properties was observed and just 2h of milling followed by compaction was sufficient to obtain a pellet with optimal thermoelectric properties. Moreover, increasing sinter temperature/time deteriorated carrier concentration hence degrading the electronic properties. Thus, optimized thermoelectric properties were obtained for the powder consolidated at 973K/20minutes. $Mg_2Si_{0.4}Sn_{0.6}$ synthesized by mechanical alloying achieved a thermoelectric figure of merit zT_{max}~1.4.

Introduction

Thermoelectrics (TE) is a principle of reversible coupling between heat and charge flow[1]. Thermoelectric materials are used in solid state devices either to harvest waste heat for power generation or for cooling applications. These solid state thermoelectric generators (TEGs) have been utilized in lunar and planetary landers in deep space probes for extra-terrestrial flight missions and commercially, for example for cathodic protection against corrosion of gas pipelines and in thermo-generators[2, 3]. To secure a place in the market, they should be inexpensive, environmentally benign and have high conversion efficiency. Fulfilling these requirements could pave the way for their application in automotive and aviation industries since two third of the generated energy from primary sources, for example fossil fuels, is released as waste heat[4, 5]. The conversion efficiency of a TEG is governed by figure-of-merit (zT) of the employed materials, which is given by $zT = S^2\sigma T/\kappa$; where S, σ, T, and κ are Seebeck coefficient, electrical conductivity, absolute temperature and the total thermal conductivity, respectively. The latter comprises of electronic (κ_{el}), bipolar (κ_{bip}) and lattice (κ_{lat}) contributions. Ideally to have maximum zT, a TE material should obey the concept of PGEC-*Phonon Glass Electron Crystal* i.e. it concomitantly should possess the electronic properties of an ideal crystalline (heavily doped) semiconductor and the thermal properties of a glass. However, it is observed that the interlink between the electronic parameters (S, σ, κ_{el} and κ_{bip}) as well as a significant contribution from the lattice makes it challenging to achieve zT_{avg}~1.0 for mid-temperature materials[5]. Amongst the various promising materials for inter-

mediate temperatures (500 – 800 K) such as PbTe[6], TAGS[7], Skutterudites[8], Zn_4Sb_3[9] and the half-Heuslers[10], magnesium silicide (Mg_2Si) based solid solutions (especially $Mg_2Si_{1-x}Sn_x$[11]) have attracted a fair amount of attention in the last decade. This is due to their confirmed excellent thermoelectric properties $zT_{max} \sim 1.3 - 1.5$ [11, 12], low density, elemental abundance and environmental compatibility[13].

A variety of synthesis routes have been examined such as melting of the elements[11, 14], self-propagating high temperature synthesis (SHS)[15], solid state reaction[16] or combining these techniques as steps[17] followed by a sintering process to obtain a pellet. Furthermore high energy ball milling has been utilized to synthesize Mg_2Si and its solid-solutions[18-20]. For the high temperature liquid synthesis route, precise Mg content control is challenging due to its high vapor pressure[16,21]. Mechanical alloying overcomes disadvantages of conventional synthesis mechanisms such as undesired material loss due to significant differences in the melting temperatures of the elements or chemical interaction of the melt with the crucibles/ampoules leading to off-stoichiometry and contamination. Furthermore MgO formation is often observe[21-23] which is detrimental to the electrical conductivity of the material[24]. Besides the $Mg_2(Si,Sn)$ system high energy ball milling has become a very popular technique for the synthesis of various thermoelectric materials[19, 25-28].

Several attempts to synthesize $Mg_2Si_{1-x}Sn_x$ by mechanical alloying in the past have resulted in the formation of either multi-phase or impure materials[29-34]. Only recently, high energy ball milling combined with a compaction step has been employed successfully to obtain n-type Mg_2Si as well as n- and p-type $Mg_2(Si,Sn)$[19, 20, 35, 36]. So, based on the previous reports it is clear that high energy ball milling is an efficient and attractive synthesis route, however, an understanding of $Mg_2Si_{1-x}Sn_x$ phase formation and underlying mechanism is yet missing. Therefore, a detailed phase formation analysis to comprehend the synthesis mechanism was performed. We decided to study the formation of $Mg_2Si_{0.4}Sn_{0.6}$ because this composition has shown the best thermoelectric properties for this material class[16, 37, 38].

The sintering parameters play a crucial role in obtaining phase pure and homogeneous samples, they furthermore heavily influence the TE properties of the material. For the $Mg_2Si_{0.4}Sn_{0.6}$ system there is first no detailed analysis available correlating sintering parameters with the TE properties, and second it remains unclear how sensitive the material is to the variation in these parameters. Instead, the previously reported sintering parameters differ and cause ambiguity[17, 39-42]. We have therefore systematically studied the changes that occur during sintering, and their effect on the TE properties was observed.

Experimental Section

The magnesium tin silicide solid solution was synthesized using commercially available starting elements (Mg turnings (Merck), Si (<6 mm, Chempure), Sn (<71 µm, Merck) and Sb (5 mm, Alfa Aesar)) all with purity >99.5%. A high-energy mechanical alloying mill (SPEX 8000D Shaker Mill) was employed with stainless steel vials and balls. The elements were weighed according to the desired composition $Mg_2Si_{1-x-y}Sn_xSb_y$ (x = 0.6, y = 0.015). Magnesium was taken 3 at.% in excess to compensate for possible Mg loss. There were two sets of experiments performed. In the first set, a specific amount of powder (1.25 g) was removed for the analysis of the sample (XRD, SEM and particle size analysis), thus as the milling progressed the ball-to-powder ratio (BPR) increased, see electronic supplementary information (Table S1 in ESI). In the second set the effect of milling time (rather than BPR) with constant BPR and $t_{milling}$ = 2 h, 4 h, 20 h, 50 h was investigated. All the samples were sintered at 973 K for 20 minutes.

In order to obtain homogeneous samples with optimum thermoelectric properties, different combinations of sintering parameters were tested. The powder mechanically alloyed for 20 hours was utilized for this

optimization study as this duration has been reported frequently in the literature[20, 35, 36, 43]. The powder handling during synthesis was done under argon to prevent oxidation and contamination. The sample powder was sintered at three different temperatures/constant time (923 K / 20min, 973 K / 20 min and 1023 K / 20min) combinations with constant temperature/different sintering times (973 K / 5 min, 973 K / 10 min, 973 K / 20 min, 973 K / 30 min) to study the effect of varying sintering parameters. Powder samples were sintered utilizing a Direct-Current Sintering Press (DSP 510 SE) from Dr. Fritsch GmbH. Sintering was performed using a graphite mold Ø12.7 mm under vacuum (~10^{-5} bar) at a heating rate of 1 K/s. The density measurement for all the pellets was done using Archimedes method. The relative densities of the obtained pellets were >95% of the theoretical value (3.06 g cm^{-3}).

X-ray diffraction was performed on powders and sample pellets utilizing a Siemens D5000 Bragg–Brentano diffractometer with a secondary monochromator. The specifics used in the system were Cu-K_α radiation (1.5406 Å) in the range (2θ: 20°–80°) with a step size of 0.01°. Scanning electron micrographs (SEM) were taken using a Zeiss Ultra 55 equipped with an energy dispersive X-ray (EDX) detector. A laser-assisted particle size analyzer (Beckman Coulter IS3320) was used to analyze the particle size distribution of powder samples. The homogeneity of sample pellets was studied by an in-house developed surface-scanning Seebeck microprobe[44]. Also, the temperature dependent electronic transport properties were measured utilizing an in-house developed facility utilizing a four-probe technique[45, 46]. The thermal diffusivity (α) of the pellets was obtained using the Netzsch LFA 427 apparatus. The thermal conductivity (κ) was obtained using the relation: $\kappa = \alpha \cdot \rho \cdot C_p$, where ρ and C_p are sample density and Dulong-Petit heat capacity. The C_p value was obtained from the Dulong-Petit limit for c_V^{DP}: $C_p = c_V^{DP} + \frac{9E_t^2 T}{\beta_T \rho}$, E_t~2×10^{-5} K^{-1} and β_T~2.07×10^{-11} Pa^{-1} are the linear coefficient of thermal expansion and isothermal compressibility, respectively[47]. The measurements were performed in a temperature range from 300 K – 773 K under vacuum. The measurement uncertainties for S, σ and κ are ± 5 %, ± 5 % and ± 8 %, respectively. For better visibility of the TE data the error bars are shown for one sample only. The room temperature Hall coefficient R_H for different samples was determined using an in-house facility in a van der Pauw configuration under a varying magnetic field of maximum 0.5 T[48]. The Hall carrier concentration n_H was estimated from R_H assuming a single carrier type $n_H = \frac{1}{R_H \times e}$. Measurement uncertainties for n_H and mobility μ_H are ± 10 %.

Results

The synthesis conditions and representative data for different samples are summarized in **Table 1**.

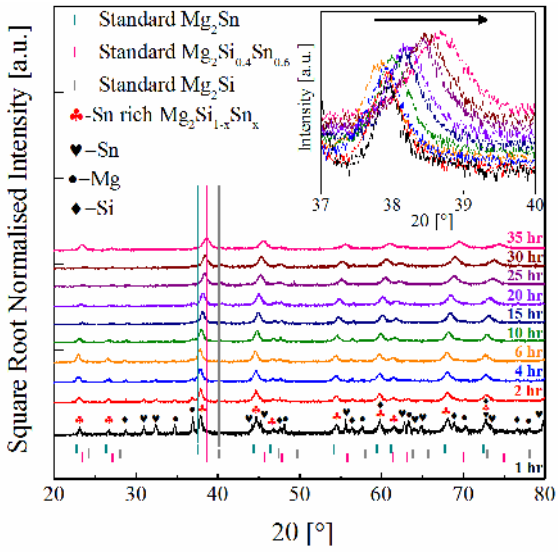

Figure 1. X-ray patterns show the formation of the desired phase with increasing milling time. A shift of the prominent (220) peak with increasing milling time can be observed from the inset [2θ ~ 37°–39°] signifying that the material system is close to the desired phase after 35 h of milling.

Table 1: Synthesis conditions, zT_{max} and room temperature carrier concentration n_H and mobility μ_H of the $Mg_2Si_{0.4}Sn_{0.6}$ samples

Sample Name	Milling time (h), Sintering temperature / time (K / min)	Density ($g \cdot cm^{-3}$)	$zT_{max.}$	n_H ($\times 10^{20}$) (cm^{-3})	μ_H ($cm^2 \cdot V^{-1}s^{-1}$)
MS – 2 – 973 / 20	2, 973 / 20	3.02 (98.6%)	1.35±0.18 (729 K)	2.3	54
MS – 4 – 973 / 20	4, 973 / 20	2.93 (95.7%)	1.37±0.19 (726 K)	2.0	51
MS – 20 -973 / 20	20, 973 / 20	2.97 (97.0%)	1.38±0.19 (759 K)	2.1	51
MS – 50 – 973 / 20	50, 973 / 20	2.95 (96.4%)	1.28±0.17 (726 K)	2.2	52
MS – 20 – 923 / 20	20, 923 / 20	3.02 (98.6%)	1.28±0.17 (779 K)	2.4	50
MS – 20 – 1023 / 20	20, 1023 / 20	2.94 (96.0%)	1.18±0.16 (759 K)	1.9	50
MS – 20 – 973 / 5	20, 973 / 5	2.98 (97.3%)	1.34±0.18 (756 K)	2.3	50
MS – 20 – 973 / 10	20, 973 / 10	2.98 (97.3%)	1.31±0.18 (759 K)	2.1	47
MS – 20 – 973 / 30	20, 973 / 30	3.03 (99.0%)	1.21±0.16 (760 K)	1.9	48

XRD patterns of the powders milled for different durations are presented in **Figure 1**. The formation of multiphase material with compositions close to Mg_2Sn takes place within the first hour, while the formation of Si-rich $Mg_2(Si,Sn)$ is not observed. The participation of starting elements in the phase formation is visualized by the diminishing elemental peaks. However, the consumption time of the starting elements is different: while Sn has basically disappeared after $t_{milling} = 15$ h, elemental Si still persists in the pattern at least until $t_{milling} = 25$ h, asserting that incorporation of Si in the material system to form the Mg-Si-Sn phase takes place after longer milling time. A gradual shift of the $Mg_2(Si,Sn)$ peaks towards higher 2θ (~37°→39° for the 220 peak) with increasing ball milling time signifies decreasing lattice constant (**Figure 1** (inset)). Any impurity peaks corresponding to phases originating from the milling vial or grinding media were not found. The median of the particle size distribution decreases with increasing milling time (**Figure 2**). Initially (up to $t_{milling} \approx 6$ h) a strong decrease in particle size is observed, mainly due to fracturing of the starting elements. The curve corresponding to powder milled from 4 h to longer milling times have increasing fraction of particles in the sub 10 micron region which is not observed for the shorter milled powders which is further followed by a plateau between $10\text{ h} - 25\text{ h}$ (the particle size distributions for exemplary powder samples is provided in Fig. S1 in the ESI). This is because the system tends to form a dynamic equilibrium between the reduction in particle size and re-agglomeration. On continuously milling, the ductile phase particles get work hardened. Later, this work hardened system undergoes progressive brittle cracking and/or further fragmentation of fragile components leading to a decrease in particle size for $t_{milling} > 25$ h.

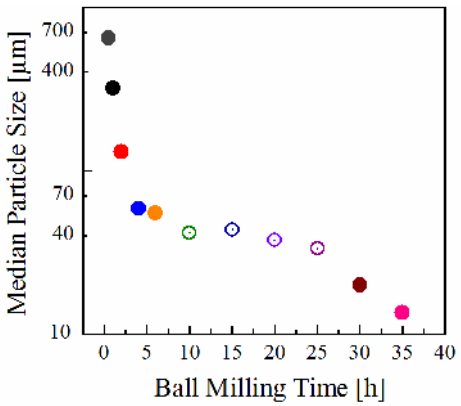

Figure 2. Particle size median versus ball milling time. Particle size decreases with longer milling time. Curve shows a plateau from 10 h to 25 h attributed to a dynamic equilibrium existing between cold welding of ductile phase particles (here Mg-Sn) and comminution of brittle phase particles (Si particles).

The SEM analysis was performed on the cross section of the powder particles milled for $t_{milling}$ = 4 h, 20 h and 35 h as shown in **Figure 3**. The observations from 4 h milled powder suggest that individual particles comprise of different starting particles cold welded together. The EDAX analysis suggests that the Mg particles preferentially tend to interact with Sn particles. The area on which the EDAX mapping and line scans were done shows that the Si particles get trapped within Mg-Sn rich particle matrix. Further investigations on 20 h milled powder particles show significant size reduction in comparison to the 4 h milled powder. The line scans performed on the Mg – Si / (Mg – Sn) – Si interfaces on the particles show that the Si concentration in the corresponding rich area decreases and the Mg and Sn concentrations become significantly larger in comparison to the 4 h milled sample. Similarly, the investigations on 35 h milled powder suggested less Si rich areas on the powder particle compared to 20 h milled powder sample. Although the Si rich region had atomic fraction(s) almost comparable to those for 20 h samples but some areas appeared to be diffusing into the Mg – Sn matrix. The additional line scans corresponding to $t_{milling}$ = 4 h, 20 h, and 35 h are also provided in the ESI (Fig. S2, S3, S4).

Discussion

The combined analysis of SEM, XRD and particle size gave us an understanding of the phase formation of $Mg_2Si_{1-x}Sn_x$ using high energy ball milling which is depicted in **Figure 4**. The cold welding and fracturing to a large extent depends on the deformation characteristics of the starting materials. Mg and Sn are ductile elements with lower shear modulus, Young's and bulk modulus compared to the more brittle silicon[49, 50] . During the complete process of mechanical alloying first, the ductile Mg and Sn dominantly experience plastic deformation (repeated cold welding and flattening) resulting in the formation of *fresh* interfaces. These new interfaces act as centers for the other elements to cold weld. On the other hand, the silicon particles are initially subject to comminution and mostly get trapped within these flattened Mg and Mg – Sn constituents. Additionally, the Si owing to higher values of moduli require either higher impact energy from the balls or longer impact time to diffuse into the complete Mg-Sn rich particle matrix as the milling progresses. Thus, the reaction time towards the desired phase gets prolonged (compared to e.g. Mg and Sn only, see ref.[30]).

With increasing milling times the Sn-rich $Mg_2Si_{1-x}Sn_x$ particles get work hardened, which increases the brittleness of the system together with the progressing Si incorporation. From this stage, the size of powder particles decreases further. Simultaneously, the Si particles get completely diffused into the Mg-Sn rich matrix leading to the formation of $Mg_2Si_{1-x}Sn_x$ solid solution with $0 < x < 1$. This is in agreement with previous reports on mechanical alloying of Mg_2X (X: Si, Sn and Ge) based materials[19, 30, 51] where the formation of Mg_2Sn comprising of ductile-ductile constituents was found to be comparatively faster than Mg_2Si (ductile – brittle system). Moreover, the experimental and theoretical values of the formation enthalpy of Mg_2Sn: -80.75 kJ/mol and -80 kJ/mol (at 298 K)

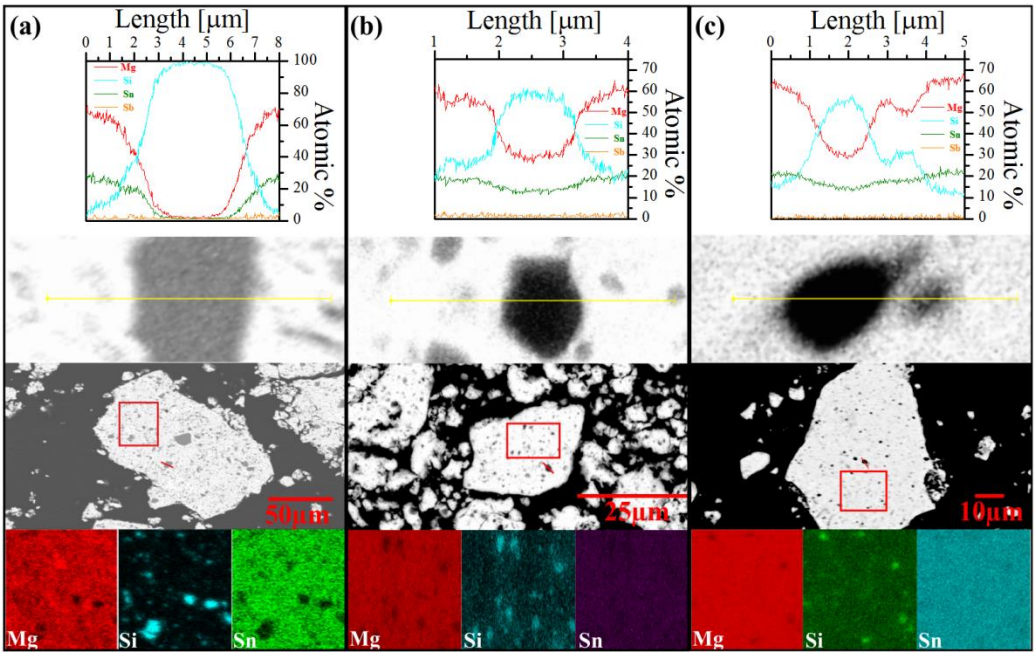

Figure 3. Electron micrographs, EDAX line scans and elemental mapping of (a) 4 h (b) 20 h and (c) 35 h milled powders.

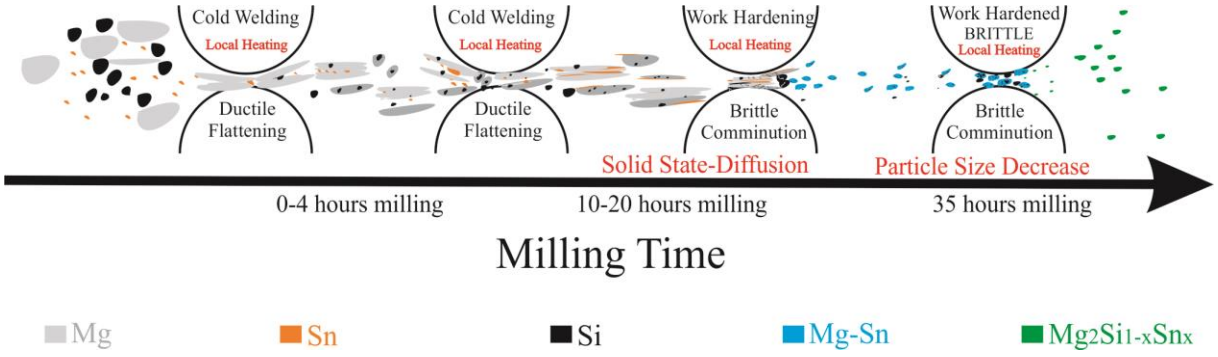

Figure 4. Formation mechanism of $Mg_2Si_{1-x}Sn_x$ phase through high energy mechanical alloying.

respectively are higher than those of Mg_2Si (-68 kJ/mol, -64.8 kJ/mol (at 298 K)) respectively[30, 52, 53] which suggests the formation of Mg_2Sn to be thermodynamically more favorable. Therefore, the observed faster (Mg – Sn) formation is also expected from a thermodynamic point of view. The cross section image of the 4 h milled powders (in **Figure 3a**) and the line scan on the highlighted region of particle shows a clear gradient in the atomic fraction. The brighter region is Mg – Sn rich whereas the dark grey area is Si rich. The gradient in atomic fraction curve is more evident at the Mg – Sn / Si interface suggesting that the diffusion of Si in to Mg – Sn rich matrix has not started yet. On milling for longer time, the particles appear to be smaller and of uniform size. The SEM analysis on a

20 h milled powder particle shows less grey areas suggesting that less Si particles are occluded by the ductile phase. The EDAX line scans on these powder particles show an increase in atomic fraction of Mg and Sn in the Si - rich particle compared to 4 h milled powder particles (**Figure 3b**). This indicates an onset but slow diffusion of silicon into the Mg – Sn matrix. This also implies that the intermetallic Mg_2Si formation at the Mg – Si interface readily takes place but the interdiffusion of ductile-brittle constituents requires prolonged mechanical force for the reaction to proceed. It can be visualized by the X-ray pattern corresponding to the 1 h milled sample showing some reflections corresponding to Mg_2Si either being Mg - or Si – rich (**Figure 1**). This is also supported by a previous report[30]. In addition to this, Aizawa et. al. found Si particles trapped in ductile matrix sustain lower strain when milled for longer time even when experiencing the same mechanical stress/force). This is because Si particles become mobile together with plastically deformed ductile constituents and experience a lower flow stress[51]. But on longer milling ($t_{\text{milling}} \geq 25$ h), the short range diffusion in the ductile matrix was evident from the diminishing Si peaks from the X-ray pattern and lowering of Si rich areas from the EDAX maps on 35 h milled powder. The dark Si rich regions had atomic fractions comparable to those found on the 20 h sample as evident from EDAX maps. Furthermore, the increase in the atomic fraction of Mg and Sn in Si rich area(s) observed from the line scans on dark (~2μm scan length) and light grey areas (at ~3 – 4μm scan length) asserts *slow* diffusion of Si in Mg-Sn matrix as (**Figure 3(c)**). This also confirms that most of the Si diffusion into Mg – Sn rich particle matrix took place almost completely. Thus, this led to formation of desired the $Mg_2Si_{1-x}Sn_x$ composition (with varying x). This is evident from the X – ray pattern of 35 h milled samples having convoluted peaks at $2\theta \sim 37.5^{\circ}$ as shown in **Figure 1**.

However, a single phase sample is achieved only after a high temperature sintering step (see Fig. S6 in the ESI).

- **Effect of milling time on thermoelectric parameters**

In order to determine the minimum milling time required to obtain phase pure material after sintering, the starting elements were mechanically alloyed for different times ($t_{\text{milling}} = 2$ h, 4 h, 20 h and 50 h). The ball-to-powder ratio was kept almost constant for all the powders (1.6:1 for $t_{\text{milling}} = 2$ h, 20 h and 50 h and 2.2:1 for $t_{\text{milling}} = 4$ h). Please note that the previously discussed powders were obtained with a strongly increasing ball-to-powder ratio and the times are therefore not directly comparable. The X-ray data asserts that a phase pure sample was obtained after sintering the powder material milled for 2 h (**Figure 5a**) already. Accordingly, samples from longer milled powder are also phase pure and the XRD patterns are nearly identical. The diffractograms of the sample pellets were indexed with standard $Mg_2Si_{0.4}Sn_{0.6}$ pattern (ICSD PDF Number: 01-089-4254) confirming the formation of desired solid solution phase (fcc, space group: Fm – 3m). Also, the samples show no MgO impurity, which is often observed for other synthesis procedures. The SEM and EDAX mapping on the MS – 20 – 973 / 20 sample showed that the sample was homogeneous. The grain boundaries were quite visible and the grain sizes were in the range of 4 – 6 μm. We found that the sample had evenly distributed elemental constituents, though Si – rich areas in the matrix are visible (**Figure 5b, 5c**). The obtained pellet was dense with little porosity. The surface Seebeck scans performed on the top and bottom surfaces of the sample revealed the homogeneity of the sample. The sample was found to be homogeneous in terms of room temperature Seebeck values (top surface: 132.1 ± 2.6 $\mu V \cdot K^{-1}$ and bottom surface: 132.2 ± 2.6 $\mu V \cdot K^{-1}$). The values are in agreement with the room temperature data of the integral temperature dependent measurements.

The transport properties of samples obtained from the 2nd set of synthesis in the temperature range 350 K – 735 K are shown in **Figure 6**.

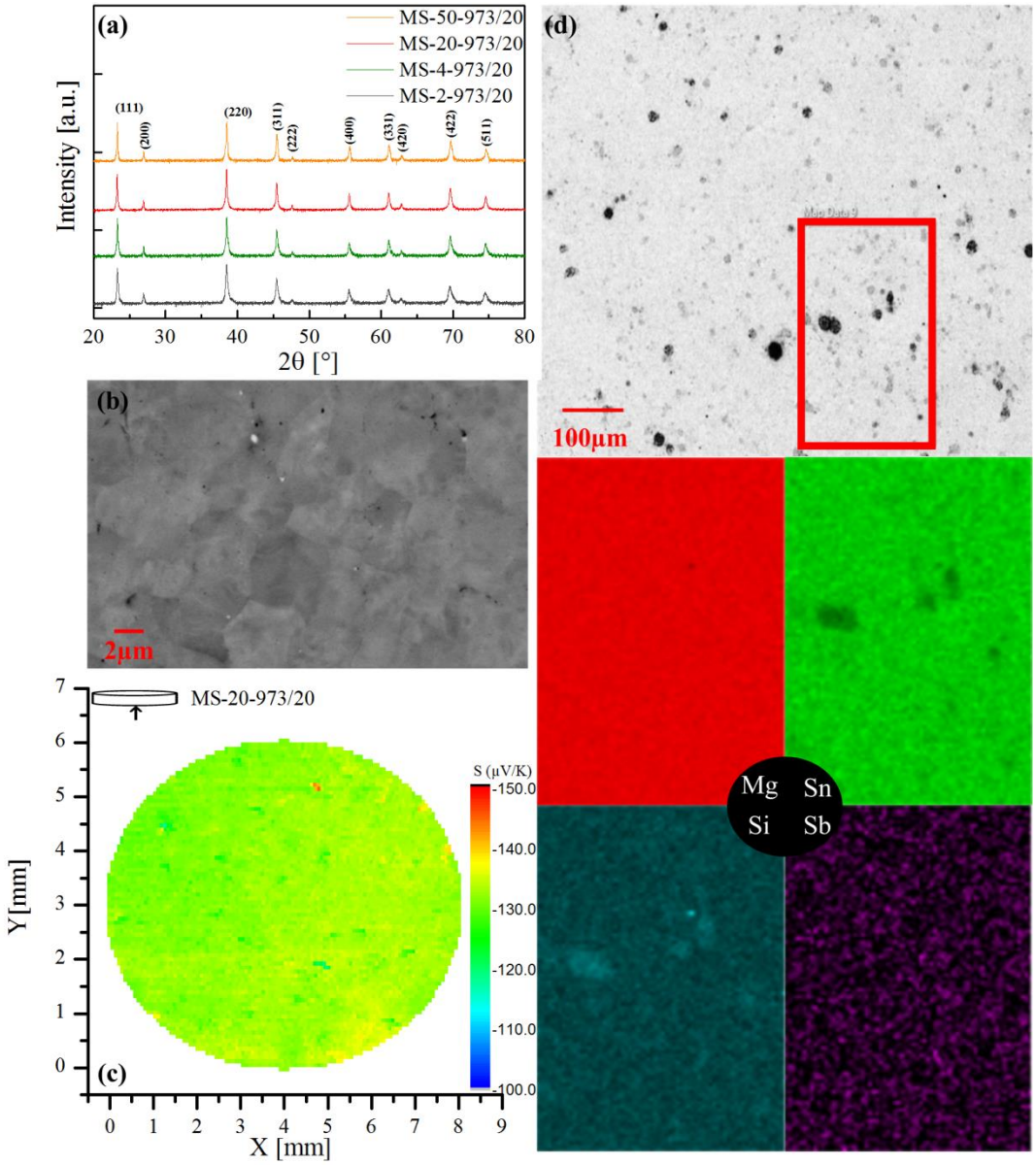

Figure 5. (a) XRD for samples with identical compaction parameters but different milling times, (b) microstructure, (c) surface Seebeck scan and (d) EDAX mapping of the compacted pellet MS – 20 – 973 / 20.

The lattice thermal conductivity plus the bipolar contribution ($\kappa - \kappa_{el}$) was calculated using $\kappa_{lat} + \kappa_{bip} = \kappa - \kappa_{el} = \kappa - L \cdot \sigma \cdot T$, where κ_{el} is the electronic contribution to the thermal conductivity and the Lorenz number (L) was calculated using the Seebeck coefficient values[54]. The Seebeck coefficient shows n-type behavior signifying electron dominated transport. Correspondingly, the electrical conductivity decreases with increasing temperature. Thus all the samples show degenerate semiconducting behavior. The high values of Seebeck coefficient -125 $\mu V \cdot K^{-1}$ and electrical conductivity 1560–1700 $S \cdot cm^{-1}$ at 350 K are attributed to the high carrier concentration combined with a large density of states carrier effective mass due to the band convergence at that composition[11, 16]. At higher temperatures (~730 K), the Seebeck coefficient increases (-225 $\mu V \cdot K^{-1}$) and electrical conductivity corres-

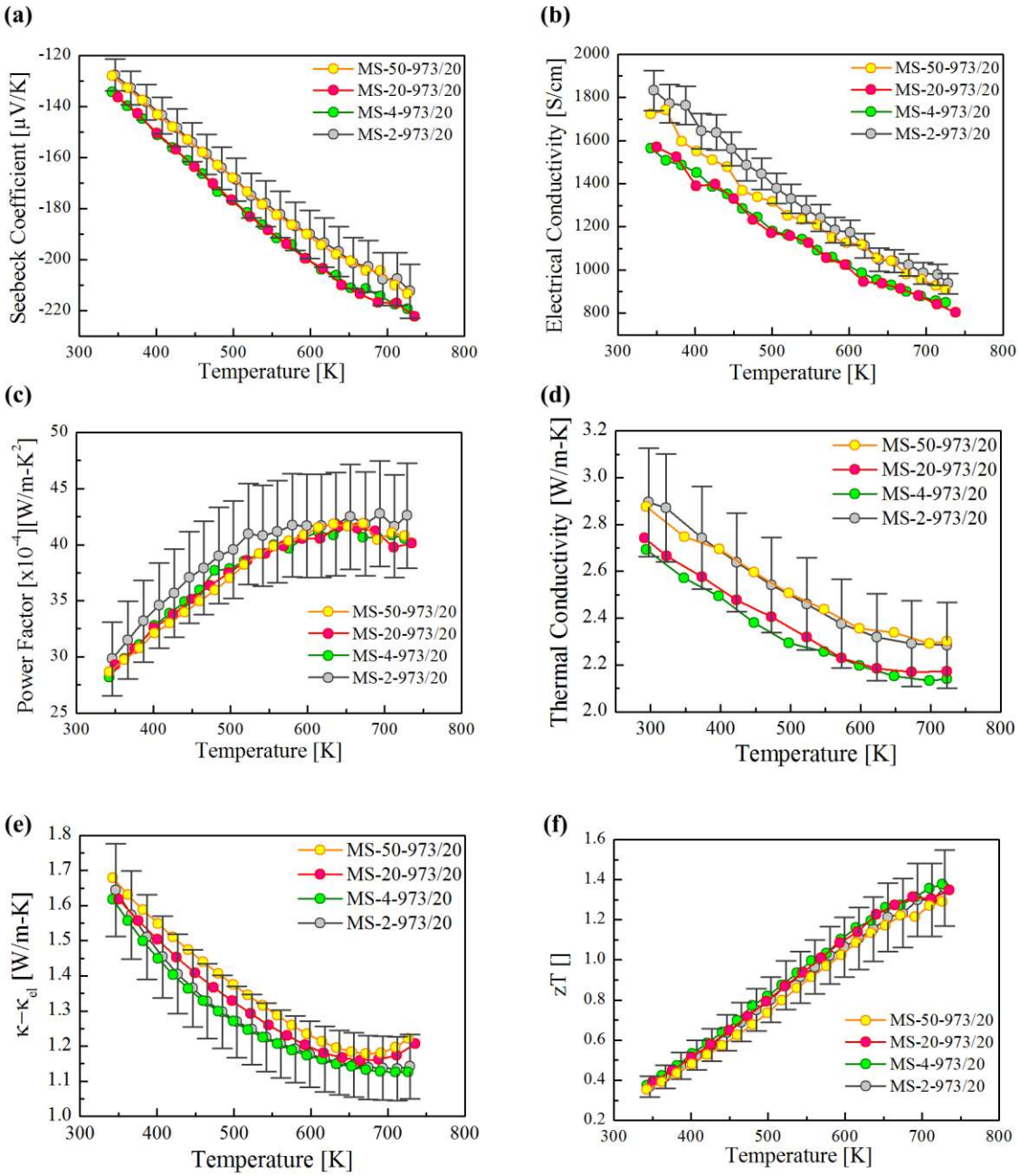

Figure 6. Thermoelectric properties of differently long (2 h, 4 h, 20 h and 50 h) milled powder samples. Fluctuations in the electronic properties can be observed but no systematic trend with increasing milling time. In particular, κ-κ_{el} remains almost unchanged.

-pondingly decreases to 800 – 930 S·cm^{-1} due to acoustic phonon scattering and alloy scattering of the charge carriers. Small and non-systematic differences can be observed between the samples, which can be attributed to small variations in carrier concentration (±10%), see **Table 1**. Nevertheless, the power factor lies in the same range for all the samples with maximum value of 39 – 42 [× 10^{-4}] W·m^{-1}·K^{-2} within the temperature region 600 – 700K.

The total thermal conductivity expectedly decreased with increasing temperature for all the samples. The bipolar effect observed in the calculated ($\kappa - \kappa_{el}$) plot was stronger for the MS – 20 – 973 / 20 and MS – 50 – 973 / 20 samples at temperature values >650 K. The results for the

lattice thermal conductivity indicate no significant effect of ball milling time. The observed small differences in the total thermal conductivity are due to the electronic contribution of the thermal conductivity of respective samples. The zT_{max} for all of the samples is tabulated in **Table 1** (zT_{max}~1.4). It is now thus demonstrated that the thermoelectric properties remain unaffected by milling for higher times.

The room temperature carrier concentration values summarized in **Table 1** were calculated from the Seebeck coefficient values using a single parabolic band (SPB) model. We have employed an average value for the density of states effective mass ($m_D^* = 2.3\ m_0$) after conducting room temperature Hall measurements on several samples of the present study. The assumption of a constant m_D^* is reasonable due to the relatively narrow carrier concentration interval; the value is furthermore in agreement with previous reports[38, 55]. The calculated Hall mobility (μ_H) is also tabulated (**Table 1**) and ranges between 50 ± 5 $cm^2 \cdot V^{-1}s^{-1}$. The values of n_H and μ_H are comparable to those reported by Farahi et. al.[17] for $Mg_2Si_{0.3}Sn_{0.665}Bi_{0.035}$ and Liu et. al.[16] for $Mg_{2.14}Si_{0.39}Sn_{0.6}Sb_{0.009}$ samples. The observed differences in electrical conductivity are mainly due to differences in n_H. This also indicates that high energy mechanical alloying does not cause a visible reduction in the carrier mobility of the $Mg_2Si_{1-x}Sn_x$ solid solutions compared to high temperature synthesis routes. This is in contrast to the observed mobility values reported for $(Bi,Sb)_2(Se,Te)_3$ solid-solutions and bulk Si samples, which decreased down on mechanical alloying[56, 57]. Furthermore, the expected decrease of lattice thermal conductivity with higher milling time was not observed and remained constant. The grain size of MS – 2 – 973 / 20 sample was 4 – 7 μm comparable to MS – 20 – 973 / 20 (4 – 6 μm) which could be a possible reason for no observable difference in the lattice thermal conductivity values (please refer to Fig. S5 in ESI). The zT_{max} values shows that high performance $Mg_2(Si,Sn)$ can be synthesized after only 2 h of mechanical alloying.

- **Effect of sintering parameters on Thermoelectric Properties:**

As discussed above a sintering step is necessary to obtain phase pure $Mg_2(Si,Sn)$. Powder compaction is sensitive to sintering parameters, namely to ramp up / down temperature, holding time, pressure (or load), sintering atmosphere etc. We have studied the effect of sintering parameters in two sets of experiments, adjusting sintering temperature in the first set while varying sinter holding time in the second. The various combinations are listed in **Table 1**. The pressure was kept constant for all the experiments (67 MPa) since no strong influence of sintering pressure on the TE properties was observed for this class of materials[58].

I. Effect of sintering temperature at constant time

The transport properties of the samples sintered for 20 min at different temperatures (MS – 20 – 923 / 20, MS – 20 – 973 / 20 and MS – 20 – 1023 / 20) were acquired after sintering the powder obtained by mechanical alloying for 20 h, see **Figure 7**. The Seebeck coefficient increased and electrical conductivity vice-versa experienced a reduction with increase in temperature. The relatively high PF value of MS – 20 – 923 / 20 is due to slightly higher carrier concentration than that of MS – 20 – 973 / 20 and MS – 20 – 1023 / 20 samples. The results for κ differ due to different electrical conductivities and differences in the lattice thermal conductivity which do not follow a discernable trend. The bipolar contribution is clearly visible above 600 K and comparable for all samples. In summary, MS – 20 – 973 / 20 display the best performance with $zT_{max} = 1.38 \pm 0.19$.

II. Effect of Sintering Time at Constant Temperature

This study was performed to identify the required sinter holding time after determining the appropriate sinter temperature. The thermoelectric data is presented in **Figure 8**. The electronic properties and lattice thermal conductivity were affected similarly to the varying

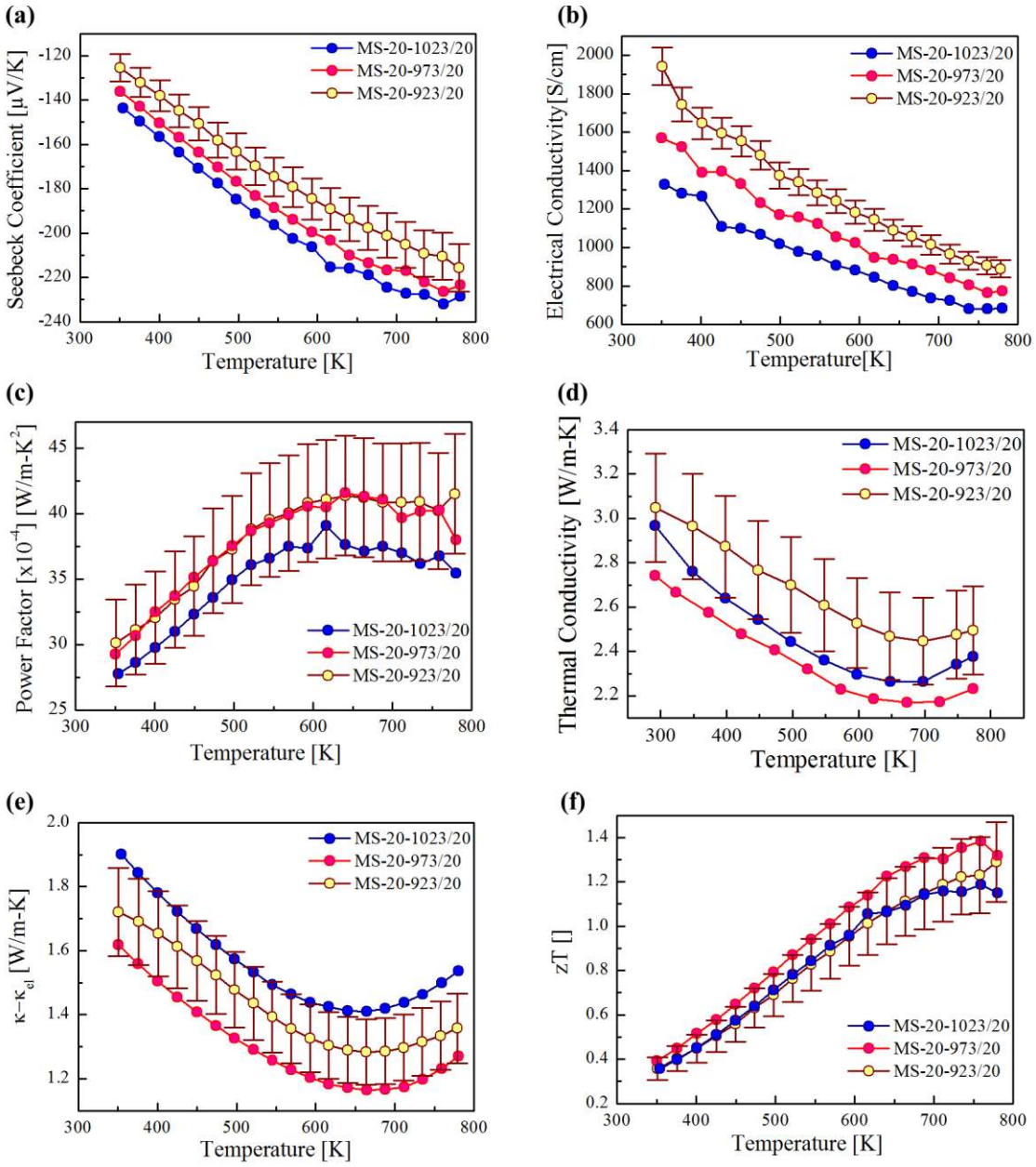

Figure 7. Thermoelectric properties of the samples sintered at different temperatures (923 K, 973 K, 1023 K) for $t_{sinter.}$=20 min. The nomenclature of the sample is MS-20-$T_{sinter.}$ / $t_{sinter.}$

temperature study. The (absolute) Seebeck coefficient values show a slight increase with increasing time of compaction, while the inverse trend is observed for the electrical conductivity data. This is in line with the observed decreasing carrier concentration, see **Table 1**. The samples compacted under a holding time of 5 and 30 minutes thus have slightly lower PF values. The loss of charge carriers at higher holding time could be attributed to the migration of antimony to the grain boundaries. The lattice thermal conductivity shows an overall increase with increasing sintering time and the bipolar contribution is roughly comparable for all samples. Although the overall thermoelectric performances of the 5, 10 and 20 min samples are comparable, we choose 20 min as preferred sintering time due to the better sample homogeneity (see Seebeck scan in **Figure 5** and Figure S7 in ESI).

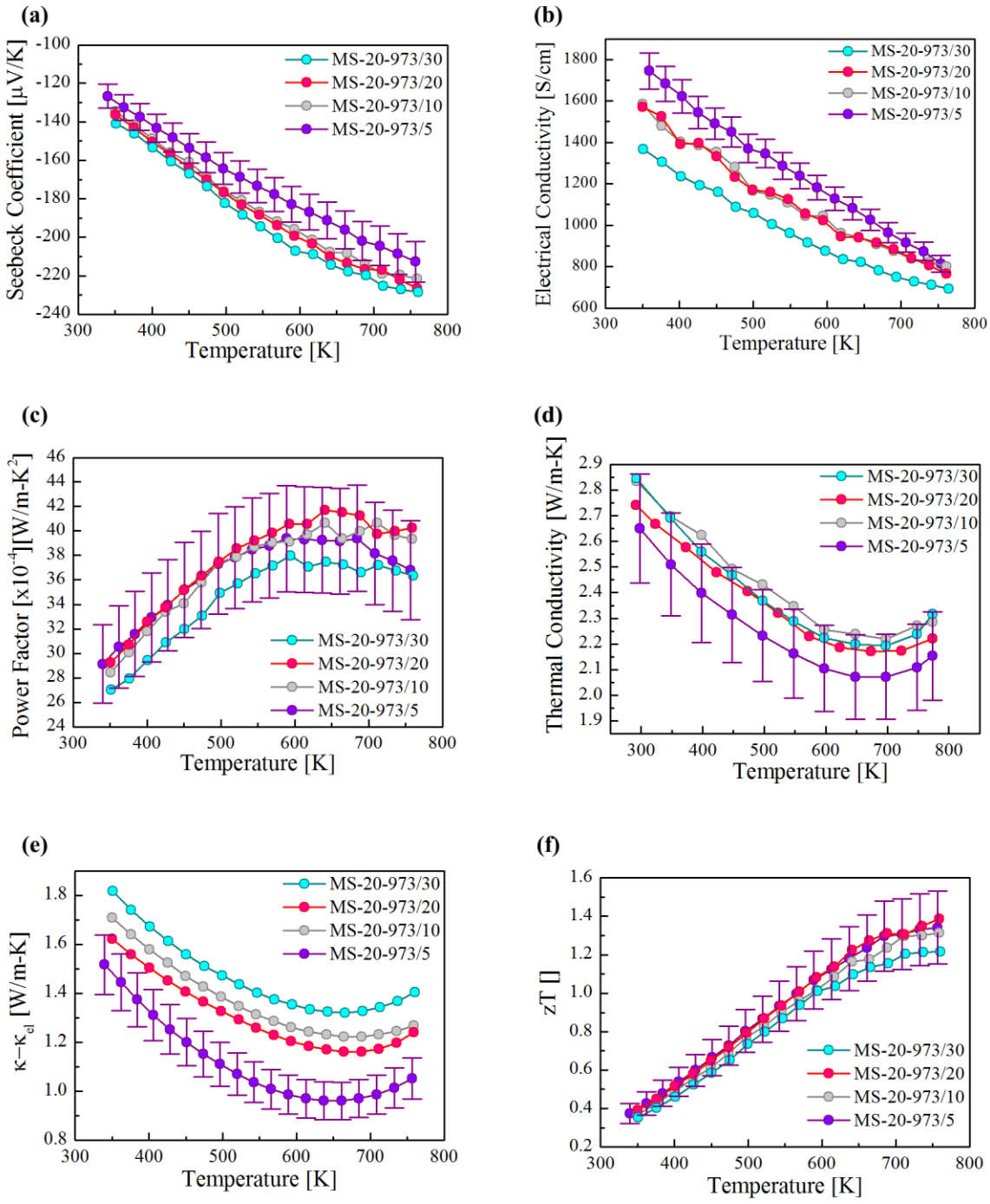

Figure 8. Thermoelectric properties of the samples sintered at $T_{sinter.}$= 700 °C for varying $t_{sinter.}$ (5, 10, 20 and 30 minutes).

Discussion

The effect of sintering temperature and time on carrier concentration and $\kappa - \kappa_{el}$ of different samples is summarized in **Figure 9**. The carrier concentration decreases with increasing sintering temperature, affecting the electronic properties. For our samples we find that increasing sintering time decreases the carrier concentration out of the optimum range thus leading to lower power factor values. The $S^2\sigma$ values of MS – 20 – 923 / 20 and MS – 20 – 973 / 20 (41.5×10^{-4} W·m^{-1}K^{-1}) were comparable to the literature values[21]. Similarly, the effect of sinter holding time is shown in **Figure 9(b)**. The increasing sintering time affected n_H leading to slightly lower power

factor values for both the 5 min and 30 min sintered samples. The observed effect of sintering time and sintering temperature is presumably a consequence of dopant segregation at the grain boundaries. It has been observed experimentally that heavy dopants (such as Sb, Bi) can migrate and settle at the grain boundaries[17]. We observe a small overall increase in lattice thermal conductivity with increasing sintering time and temperature. The reason for that remains to be found but is not an obvious grain growth. The absolute value of $\kappa - \kappa_{el}$ for the samples $(1.5 \pm 0.1 - 1.8)$ is comparable to those reported by Farahi et. al. for $Mg_2Si_{0.365}Sn_{0.6}Bi_{0.035}$ (1.39 $W{\cdot}m^{-1}K^{-1}$ at 320K)[17] and calculated values by Tan et. al. for $Mg_2Si_{0.365}Sn_{0.625}$ showed $\kappa - \kappa_{el}$~1.62 $W{\cdot}m^{-1}K^{-1}$ (at 300 K)[59]. Overall, it was observed that two hours of milling is enough to obtain a phase pure pellet. The thermoelectric properties are almost unaffected by increasing the milling time. The thermoelectric performance of the best samples is found to be competitive to some other previously reported studies for the same material[21, 38] utilizing different synthesis procedures. The ambiguity that arose as a result of reports of different sintering conditions for $Mg_2Si_{0.4}Sn_{0.6}$ material(s)[17, 39, 41, 60] is resolved by a detailed study on varying time and temperature in different combination. The increase in sintering temperature and time was observed to affect the carrier concentration and lattice thermal conductivity of different samples leading to changes in the thermoelectric properties. Nevertheless the zT_{max} of different samples was found to vary between 1.2 - 1.4 suggesting that the thermoelectric properties of Mg_2X solid solutions are quite robust with respect to the synthesis parameters.

This is in contrast to other material system, where the thermoelectric properties were found to be more sensitive to the compaction parameters, e.g. $CoSb_3$ based Skutterudites[61], Zn_4Sb_3 [62] and $AgSn_mSbTe_{2+m}$ materials[63].

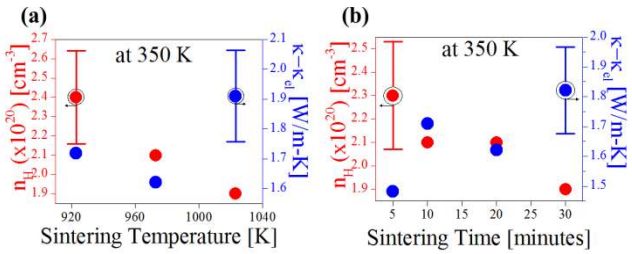

Figure 9. Plots showing change in carrier concentration (n_H) and lattice thermal conductivity ($\kappa - \kappa_{el}$) on varying (a) sintering temperature ($t_{sinter.}$- 20 minutes) (b) sintering time ($T_{sinter.}$ 973 K).

Conclusion

The formation mechanism of $Mg_2Si_{0.4}Sn_{0.6}$ by mechanical alloying was investigated. Initially Sn-rich $Mg_2(Si,Sn)$ is formed followed by the slow incorporation of Si driving the composition towards the desired $Mg_2Si_{0.4}Sn_{0.6}$ phase. This is supported by the XRD peak shift towards higher angles and an increasing homogenization as observed from the cross-sectional SEM images of the powder. However, we also find that within the observed milling time no phase pure $Mg_2Si_{0.4}Sn_{0.6}$ was obtained by high energy mechanical alloying only, but rather a somewhat broad phase mixture. In order to obtain a phase pure pellet a high temperature sintering step is required. We have therefore shown that the $Mg_2Si_{0.4}Sn_{0.6}$ material synthesis is a two-step process involving high energy mechanical alloying and high temperature pressing of the mechanically alloyed powder. We have found the same phenomenon experimentally also for other ternary compositions of (Mg_2Si,Sn) in contrast to previous reports on binary Mg_2X (X: Si, Sn, Ge). Investigations on the phase pure samples synthesized by mechanical alloying for different milling time ($t_{milling}$ = 2 h, 4 h, 20 h, 50 h) led to the conclusion that two hours of mechanical alloying is sufficient and no significant influence of milling time on the TE properties was found. On the other hand, systematic effects of the sintering parameters were observed: An increase in sintering time and temperature lead to a shift of optimum carrier concentration and hence caused changes in the electronic proper-

ties. In contrast, the thermal properties showed an increasing trend while tuning these parameters. This also suggests that the grain size does not change a lot and is large enough to cause any significant effect on thermal properties of Mg_2X based solid solutions. In summary, we found the optimum thermoelectric properties for sintering at 973 K for 20 minutes. We also found that the synthesis route has a good reproducibility and is relatively robust against small changes of the synthesis parameters. Mechanical alloying is thus a sound and attractive technique that can be utilized for high performance Mg_2X based solid solutions.

ASSOCIATED CONTENT

Supporting Information.

The supporting material is available free of charge via the Internet at http://pubs.acs.org.

AUTHOR INFORMATION

Corresponding Author(s)

*E-mail: Aryan.Sankhla@dlr.de & Johannes.deBoor@dlr.de.

Author Contributions

‡Aryan Sankhla and Akash Patil contributed equally to the work.

ACKNOWLEDGMENT

The authors would like to thank P. Blaschkewitz (DLR) for his untiring support with the thermoelectric measurements. The authors would also like to thank C. Stiewe and R. Sottong for their help in sample preparation for SEM characterization. The authors acknowledge Pawel Ziolkowski for his help in providing and conducting Seebeck scans on sample surface. The authors (A.S., H.K. & N.F.) would like to acknowledge financial support by the DAAD (Fellowship No.: 247 & 241) respectively. Also, financial support of one of the authors (M.Y.) is provided by the DFG via the GRK (Research Training Group) 2204 "Substitute Materials for sustainable Energy Technologies".

REFERENCES

1. Brantut, J.-P.; Grenier, C.; Meineke, J.; Stadler, D.; Krinner, S.; Kollath, C.; Esslinger, T.; Georges, A., A Thermoelectric Heat Engine with Ultracold Atoms. *Science* **2013,** 342, (6159), 713-715.

2. Tsynaeva, A. A., Cathode Protection Systems of Cross-country Pipelines. *Procedia Engineering* **2015,** 111, 777-782.

3. Beretta, D.; Massetti, M.; Lanzani, G.; Caironi, M., Thermoelectric characterization of flexible micro-thermoelectric generators. *Review of Scientific Instruments* **2017,** 88, (1), 015103.

4. Alam, H.; Ramakrishna, S., A review on the enhancement of figure of merit from bulk to nano-thermoelectric materials. *Nano Energy* **2013,** 2, (2), 190-212.

5. Snyder, G. J.; Toberer, E. S., Complex thermoelectric materials. *Nat Mater* **2008,** 7, (2), 105-114.

6. Gelbstein, Y.; Dashevsky, Z.; Dariel, M. P., The search for mechanically stable PbTe based thermoelectric materials. *Journal of Applied Physics* **2008,** 104, (3), 033702.

7. Cook, B. A.; Kramer, M. J.; Wei, X.; Harringa, J. L.; Levin, E. M., Nature of the cubic to rhombohedral structural transformation in $(AgSbTe_2)_{15}(GeTe)_{85}$ thermoelectric material. *Journal of Applied Physics* **2007,** 101, (5), 053715.

8. Tang, Y.; Gibbs, Z. M.; Agapito, L. A.; Li, G.; Kim, H.-S.; Nardelli, M. B.; Curtarolo, S.; Snyder, G. J., Convergence of multi-valley bands as the electronic origin of high thermoelectric performance in $CoSb_3$ skutterudites. *Nat Mater* **2015,** 14, (12), 1223-1228.

9. Snyder, G. J.; Christensen, M.; Nishibori, E.; Caillat, T.; Iversen, B. B., Disordered zinc in Zn_4Sb_3 with phonon-glass and electron-crystal thermoelectric properties. *Nat Mater* **2004,** 3, (7), 458-463.

10. Chen, S.; Ren, Z., Recent progress of half-Heusler for moderate temperature thermoelectric applications. *Materials Today* **2013,** 16, (10), 387-395.

11. Zaitsev, V. K.; Fedorov, M. I.; Gurieva, E. A.; Eremin, I. S.; Konstantinov, P. P.; Samunin, A. Y.; Vedernikov, M. V., Highly effective $Mg_2Si_{1-x}Sn_x$ thermoelectrics. *Physical Review B* **2006,** 74, (4), 045207.

12. Zaitsev, V., Thermoelectrics on the base of solid solutions of Mg_2B^{IV} compounds (BIV= Si, Ge, Sn). In *Thermoelectrics Handbook: macro to nano*, CRC Press: 2005; pp 29-1-29-12.

13. de Boor, J.; Dasgupta, T.; Saparamadu, U.; Müller, E.; Ren, Z. F., Recent progress in p-type thermoelectric magnesium silicide based solid solutions. *Materials Today Energy* **2017,** 4, 105-121.

14. Dasgupta, T.; Stiewe, C.; de Boor, J.; Müller, E., Influence of power factor enhancement on the thermoelectric figure of merit in $Mg_2Si_{0.4}Sn_{0.6}$ based materials. *physica status solidi (a)* **2014,** 211, (6), 1250-1254.

15. Zhang, Q.; Su, X.; Yan, Y.; Xie, H.; Liang, T.; You, Y.; Tang, X.; Uher, C., Phase Segregation and Superior Thermoelectric Properties of $Mg_2Si_{1-x}Sb_x$ ($0 \le x \le 0.025$) Prepared by Ultrafast Self-Propagating High-Temperature Synthesis. *ACS Applied Materials & Interfaces* **2016,** 8, (5), 3268-3276.

16. Liu, W.; Tan, X.; Yin, K.; Liu, H.; Tang, X.; Shi, J.; Zhang, Q.; Uher, C., Convergence of Conduction Bands as a Means of Enhancing Thermoelectric Performance of n-Type $Mg_2Si_{1-x}Sn_x$ Solid Solutions. *Physical Review Letters* **2012,** 108, (16), 166601.

17. Farahi, N.; Prabhudev, S.; Botton, G. A.; Salvador, J. R.; Kleinke, H., Nano- and Microstructure Engineering: An Effective Method for Creating High Efficiency Magnesium Silicide Based Thermoelectrics. *ACS Applied Materials & Interfaces* **2016,** 8, (50), 34431-34437.

18. Liu, W.; Kim, H. S.; Chen, S.; Jie, Q.; Lv, B.; Yao, M.; Ren, Z.; Opeil, C. P.; Wilson, S.; Chu, C.-W.; Ren, Z., n-type thermoelectric material $Mg_2Sn_{0.75}Ge_{0.25}$ for high power generation. *Proceedings of the National Academy of Sciences* **2015,** 112, (11), 3269-3274.

19. Bux, S. K.; Yeung, M. T.; Toberer, E. S.; Snyder, G. J.; Kaner, R. B.; Fleurial, J.-P., Mechanochemical synthesis and thermoelectric properties of high quality magnesium silicide. *Journal of Materials Chemistry* **2011,** 21, (33), 12259-12266.

20. Mao, J.; Kim, H. S.; Shuai, J.; Liu, Z.; He, R.; Saparamadu, U.; Tian, F.; Liu, W.; Ren, Z., Thermoelectric properties of materials near the band crossing line in Mg_2Sn–Mg_2Ge–Mg_2Si system. *Acta Materialia* **2016,** 103, 633-642.

21. Liu, W.; Tang, X.; Li, H.; Yin, K.; Sharp, J.; Zhou, X.; Uher, C., Enhanced thermoelectric properties of n-type $Mg_{2.16}(Si_{0.4}Sn_{0.6})_{1-y}Sb_y$ due to nano-sized Sn-rich precipitates and an optimized electron concentration. *Journal of Materials Chemistry* **2012,** 22, (27), 13653-13661.

22. Dasgupta, T.; Stiewe, C.; Hassdorf, R.; Zhou, A. J.; Boettcher, L.; Mueller, E., Effect of vacancies on the thermoelectric properties of $Mg_2Si_{1-x}Sb_x$ ($0 \le x \le 0.1$). *Physical Review B* **2011,** 83, (23), 235207.

23. Zhang, L.; Xiao, P.; Shi, L.; Henkelman, G.; Goodenough, J. B.; Zhou, J., Suppressing the bipolar contribution to the thermoelectric properties of $Mg_2Si_{0.4}Sn_{0.6}$ by Ge substitution. *Journal of Applied Physics* **2015,** 117, (15), 155103.

24. de Boor, J.; Dasgupta, T.; Kolb, H.; Compere, C.; Kelm, K.; Mueller, E., Microstructural effects on thermoelectric efficiency: A case study on magnesium silicide. *Acta Materialia* **2014,** 77, (Supplement C), 68-75.

25. May, A. F.; Fleurial, J.-P.; Snyder, G. J., Thermoelectric performance of lanthanum telluride produced via mechanical alloying. *Physical Review B* **2008,** 78, (12), 125205.

26. May, A. F.; Toberer, E. S.; Saramat, A.; Snyder, G. J., Characterization and analysis of thermoelectric transport in n-type $Ba_8Ga_{16-x}Ge_{30+x}$. *Physical Review B* **2009,** 80, (12), 125205.

27. Li, D.; Zhao, H.; Li, S.; Wei, B.; Shuai, J.; Shi, C.; Xi, X.; Sun, P.; Meng, S.; Gu, L.; Ren, Z.; Chen, X., Atomic Disorders Induced by Silver and Magnesium Ion

Migrations Favor High Thermoelectric Performance in α-MgAgSb-Based Materials. *Advanced Functional Materials* **2015,** 25, (41), 6478-6488.

28. Shuai, J.; Wang, Y.; Liu, Z.; Kim, H. S.; Mao, J.; Sui, J.; Ren, Z., Enhancement of thermoelectric performance of phase pure Zintl compounds $Ca_{1-x}Yb_xZn_2Sb_2$, $Ca_{1-x}Eu_xZn_2Sb_2$, and $Eu_{1-x}Yb_xZn_2Sb_2$ by mechanical alloying and hot pressing. *Nano Energy* **2016,** 25, 136-144.

29. Riffel, M.; Schilz, J. Mechanically alloyed $Mg_2Si_{1-x}Sn_x$ solid solutions as thermoelectric materials, Thermoelectrics, 1996., Fifteenth International Conference on, 26-29 March 1996, 1996; 1996; pp 133-136.

30. Clark, C. R.; Wright, C.; Suryanarayana, C.; Baburaj, E. G.; Froes, F. H., Synthesis of Mg_2X (X = Si, Ge, or Sn) intermetallics by mechanical alloying. *Materials Letters* **1997,** 33, (1), 71-75.

31. You, S.-W.; Kim, I.-H.; Choi, S.-M.; Seo, W.-S.; Kim, S.-U., Solid-State Synthesis and Thermoelectric Properties of $Mg_2Si_{1-x}Sn_x$. *Journal of Electronic Materials* **2013,** 42, (7), 1490-1494.

32. You, S.-W.; Kim, I.-H.; Choi, S.-M.; Seo, W.-S., Thermoelectric properties of Bi-doped $Mg_2Si_{1-x}Sn_x$ prepared by mechanical alloying. *Journal of the Korean Physical Society* **2013,** 63, (11), 2153-2157.

33. You, S.-W.; Kim, I.-H.; Choi, S.-M.; Seo, W.-S., Thermoelectric properties of Sb-doped $Mg_2Si_{1-x}Sn_x$ prepared by mechanical alloying and hot pressing. *Journal of Ceramic Processing Research* **2014,** 15, (6), 398-402.

34. Hu, X.; Barnett, M. R.; Yamamoto, A., Synthesis of Al-doped $Mg_2Si_{1-x}Sn_x$ compound using magnesium alloy for thermoelectric application. *Journal of Alloys and Compounds* **2015,** 649, 1060-1065.

35. Saparamadu, U.; Mao, J.; Dahal, K.; Zhang, H.; Tian, F.; Song, S.; Liu, W.; Ren, Z., The effect of charge carrier and doping site on thermoelectric properties of $Mg_2Sn_{0.75}Ge_{0.25}$. *Acta Materialia* **2017,** 124, 528-535.

36. de Boor, J.; Saparamadu, U.; Mao, J.; Dahal, K.; Müller, E.; Ren, Z., Thermoelectric performance of Li doped, p-type $Mg_2(Ge,Sn)$ and comparison with $Mg_2(Si,Sn)$. *Acta Materialia* **2016,** 120, 273-280.

37. Liu, W.; Chi, H.; Sun, H.; Zhang, Q.; Yin, K.; Tang, X.; Zhang, Q.; Uher, C., Advanced thermoelectrics governed by a single parabolic band: $Mg_2Si_{0.3}Sn_{0.7}$, a canonical example. *Physical Chemistry Chemical Physics* **2014,** 16, (15), 6893-6897.

38. Gao, P.; Berkun, I.; Schmidt, R. D.; Luzenski, M. F.; Lu, X.; Bordon Sarac, P.; Case, E. D.; Hogan, T. P., Transport and Mechanical Properties of High-ZT $Mg_{2.08}Si_{0.4-x}Sn_{0.6}Sb_x$ Thermoelectric Materials. *Journal of Electronic Materials* **2014,** 43, (6), 1790-1803.

39. Zheng, L.; Zhang, X.; Liu, H.; Li, S.; Zhou, Z.; Lu, Q.; Zhang, J.; Zhang, F., Optimized nanostructure and thermoelectric performances of $Mg_2(Si_{0.4}Sn_{0.6})Sb_x$ solid solutions by in situ nanophase generation. *Journal of Alloys and Compounds* **2016,** 671, 452-457.

40. Søndergaard, M.; Christensen, M.; Borup, K. A.; Yin, H.; Iversen, B. B., Thermal stability and thermoelectric properties of $Mg_2Si_{0.4}Sn_{0.6}$ and $Mg_2Si_{0.6}Sn_{0.4}$. *Journal of Materials Science* **2013,** 48, (5), 2002-2008.

41. Bellanger, P.; Gorsse, S.; Bernard-Granger, G.; Navone, C.; Redjaimia, A.; Vivès, S., Effect of microstructure on the thermal conductivity of nanostructured $Mg_2(Si,Sn)$ thermoelectric alloys: An experimental and modeling approach. *Acta Materialia* **2015,** 95, 102-110.

42. Wei, L.; Xinfeng, T.; Jeff, S., Low-temperature solid state reaction synthesis and thermoelectric properties of high-performance and low-cost Sb-doped $Mg_2Si_{0.6}Sn_{0.4}$. *Journal of Physics D: Applied Physics* **2010,** 43, (8), 085406.

43. Liu, Z.; Shuai, J.; Mao, J.; Wang, Y.; Wang, Z.; Cai, W.; Sui, J.; Ren, Z., Effects of antimony content in $MgAg_{0.97}Sb_x$ on output power and energy conversion efficiency. *Acta Materialia* **2016,** 102, 17-23.

44. Platzek, D.; Karpinski, G.; Drasar, C.; Muller, E., Seebeck scanning microprobe for thermoelectric FGM.

Functionally Graded Materials Viii **2005,** 492-493, 587-592.

45. de Boor, J.; Stiewe, C.; Ziolkowski, P.; Dasgupta, T.; Karpinski, G.; Lenz, E.; Edler, F.; Mueller, E., High-Temperature Measurement of Seebeck Coefficient and Electrical Conductivity. *Journal of Electronic Materials* **2013,** 42, (7), 1711-1718.

46. Boor, J. d.; Müller, E., Data analysis for Seebeck coefficient measurements. *Review of Scientific Instruments* **2013,** 84, (6), 065102.

47. Borup, K. A.; de Boor, J.; Wang, H.; Drymiotis, F.; Gascoin, F.; Shi, X.; Chen, L.; Fedorov, M. I.; Muller, E.; Iversen, B. B.; Snyder, G. J., Measuring thermoelectric transport properties of materials. *Energy & Environmental Science* **2015,** 8, (2), 423-435.

48. van der Pauw, L., A method of measuring specific resistivity and Hall effect of discs of arbitrary shape. *Philips Res. Rep* **1958,** 13, 1-9.

49. Gale, W.F, Mechanical properties of metals and alloys A2. *Smithells Metals Reference Book (Eighth Edition)*, Totemeier, T. C., Ed. Butterworth-Heinemann: Oxford, 2004; pp 22-1-22-162.

50. Hopcroft, M. A.; Nix, W. D.; Kenny, T. W., What is the Young's Modulus of Silicon? *Journal of Microelectromechanical Systems* **2010,** 19, (2), 229-238.

51. Aizawa, T.; Song, R., Mechanically induced reaction for solid-state synthesis of Mg_2Si and Mg_2Sn. *Intermetallics* **2006,** 14, (4), 382-391.

52. Song, R. B.; Aizawa, T.; Sun, J. Q., Synthesis of $Mg_2Si_{1-x}Sn_x$ solid solutions as thermoelectric materials by bulk mechanical alloying and hot pressing. *Materials Science and Engineering: B* **2007,** 136, (2), 111-117.

53. Jung, I.-H.; Kang, D.-H.; Park, W.-J.; Kim, N. J.; Ahn, S., Thermodynamic modeling of the Mg–Si–Sn system. *Calphad* **2007,** 31, (2), 192-200.

54. Kim, H.-S.; Gibbs, Z. M.; Tang, Y.; Wang, H.; Snyder, G. J., Characterization of Lorenz number with Seebeck coefficient measurement. *APL Materials* **2015,** 3, (4), 041506.

55. Jiang, G.; He, J.; Zhu, T.; Fu, C.; Liu, X.; Hu, L.; Zhao, X., High Performance $Mg_2(Si,Sn)$ Solid Solutions: a Point Defect Chemistry Approach to Enhancing Thermoelectric Properties. *Advanced Functional Materials* **2014,** 24, (24), 3776-3781.

56. Bux, S. K.; Blair, R. G.; Gogna, P. K.; Lee, H.; Chen, G.; Dresselhaus, M. S.; Kaner, R. B.; Fleurial, J.-P., Nanostructured Bulk Silicon as an Effective Thermoelectric Material. *Advanced Functional Materials* **2009,** 19, (15), 2445-2452.

57. Hu, L.; Zhu, T.; Liu, X.; Zhao, X., Point Defect Engineering of High-Performance Bismuth-Telluride-Based Thermoelectric Materials. *Advanced Functional Materials* **2014,** 24, (33), 5211-5218.

58. de Boor, J.; Compere, C.; Dasgupta, T.; Stiewe, C.; Kolb, H.; Schmitz, A.; Mueller, E., Fabrication parameters for optimized thermoelectric Mg_2Si. *Journal of Materials Science* **2014,** 49, (8), 3196-3204.

59. Tan, X. J.; Liu, W.; Liu, H. J.; Shi, J.; Tang, X. F.; Uher, C., Multiscale calculations of thermoelectric properties of n-type $Mg_2Si_{1-x}Sn_x$ solid solutions. *Physical Review B* **2012,** 85, (20), 205212.

60. Søndergaard, M.; Christensen, M.; Borup, K. A.; Yin, H.; Iversen, B. B., Gravity-induced gradients in thermoelectric $Mg_2Si_{0.9925-x}Sn_xSb_{0.0075}$. *Acta Materialia* **2012,** 60, (16), 5745-5751.

61. Liu, W.-S.; Zhang, B.-P.; Li, J.-F.; Zhao, L.-D., Thermoelectric property of fine-grained $CoSb_3$ skutterudite compound fabricated by mechanical alloying and spark plasma sintering. *Journal of Physics D: Applied Physics* **2007,** 40, (2), 566.

62. Pedersen, B. L.; Birkedal, H.; Iversen, B. B.; Nygren, M.; Frederiksen, P. T., Influence of sample compaction on the thermoelectric performance of Zn_4Sb_3. *Applied Physics Letters* **2006,** 89, (24), 242108.

63. Falkenbach, O.; Schmitz, A.; Dankwort, T.; Koch, G.; Kienle, L.; Müller, E.; Schlecht, S., Influence of mechanochemical syntheses and compacting methods on the thermoelectric properties of nanostructured

$AgSn_mSbTe_{2+m}$ (TAST-m). *Semiconductor Science and Technology* **2014,** 29, (12), 124009.

Insert Table of Contents artwork here